Since January 2020 Elsevier has created a COVID-19 resource centre with free information in English and Mandarin on the novel coronavirus COVID-19. The COVID-19 resource centre is hosted on Elsevier Connect, the company's public news and information website.

Cell Reports

Structural analysis of receptor binding domain mutations in SARS-CoV-2 variants of concern that modulate ACE2 and antibody binding

Graphical abstract

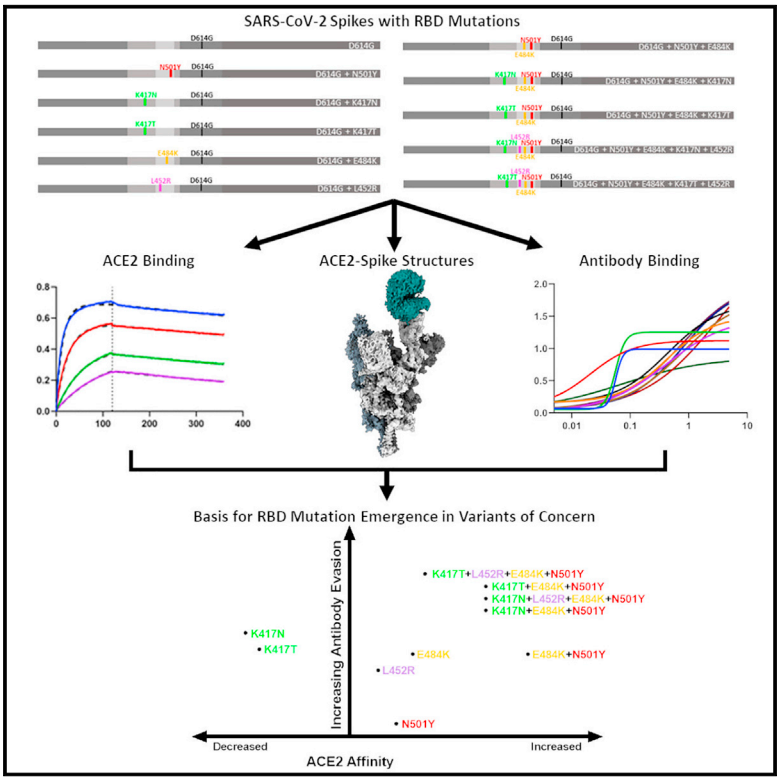

Highlights

- E484K and L452R increase ACE2 affinity and reduce antibody binding
- K417N/T mutations reduce antibody binding at a cost to ACE2 affinity
- Cryo-EM structures reveal details of ACE2 contacts with mutant spike proteins
- Analysis of ACE2 binding and antibody evasion in unnatural RBD mutational combinations

Authors

Dhiraj Mannar, James W. Saville, Xing Zhu, ..., Wei Li, Dimiter S. Dimitrov, Sriram Subramaniam

Correspondence

sriram.subramaniam@ubc.ca

In brief

Mannar et al. use structural and biochemical techniques to dissect the role of SARS-CoV-2 spike glycoprotein mutations within the receptor binding domain, demonstrating modular mutational effects that combine to simultaneously enhance receptor engagement and decrease antibody binding in emerging variant spike proteins.

Mannar et al., 2021, Cell Reports *37*, 110156
December 21, 2021
https://doi.org/10.1016/j.celrep.2021.110156

Cell Reports

CellPress
OPEN ACCESS

Report

Structural analysis of receptor binding domain mutations in SARS-CoV-2 variants of concern that modulate ACE2 and antibody binding

Dhiraj Mannar,[1,3] James W. Saville,[1,3] Xing Zhu,[1] Shanti S. Srivastava,[1] Alison M. Berezuk,[1] Steven Zhou,[1] Katharine S. Tuttle,[1] Andrew Kim,[2] Wei Li,[2] Dimiter S. Dimitrov,[2] and Sriram Subramaniam[1,4,*]

[1]Department of Biochemistry and Molecular Biology, University of British Columbia, Vancouver, BC V6T 1Z3, Canada

[2]Center for Antibody Therapeutics, Division of Infectious Diseases, Department of Medicine, UPMC, 3550 Terrace Str, Pittsburgh, PA 15261, USA

[3]These authors contributed equally

[4]Lead contact

*Correspondence: sriram.subramaniam@ubc.ca

https://doi.org/10.1016/j.celrep.2021.110156

SUMMARY

The recently emerged severe acute respiratory syndrome coronavirus-2 (SARS-CoV-2) Beta (B.1.351) and Gamma (P.1) variants of concern (VoCs) include a key mutation (N501Y) found in the Alpha (B.1.1.7) variant that enhances affinity of the spike protein for its receptor, angiotensin-converting enzyme 2 (ACE2). Additional mutations are found in these variants at residues 417 and 484 that appear to promote antibody evasion. In contrast, the Epsilon variants (B.1.427/429) lack the N501Y mutation yet exhibit antibody evasion. We have engineered spike proteins to express these receptor binding domain (RBD) VoC mutations either in isolation or in different combinations and analyze the effects using biochemical assays and cryoelectron microscopy (cryo-EM) structural analyses. Overall, our findings suggest that the emergence of new SARS-CoV-2 variant spikes can be rationalized as the result of mutations that confer increased ACE2 affinity, increased antibody evasion, or both, providing a framework to dissect the molecular factors that drive VoC evolution.

INTRODUCTION

Recent genomic surveillance efforts tracking the global spread of severe acute respiratory syndrome coronavirus-2 (SARS-CoV-2) have identified the emergence and rapid spread of several variants. Variants Alpha (B.1.1.7, first observed in the United Kingdom), VOC 202102/02, Beta (B.1.351, first observed in South Africa), Gamma (P.1, first observed in Brazil), and Epsilon (B.1.427 and B.1.429, first observed in California) have all been identified by the American Centers for Disease Control and Prevention (CDC) as either variants of concern (VoCs) or variants interest (VoIs) (CDC, 2021a). These variants are designated as having evidence demonstrating increased transmissibility, increased disease severity, and/or a significant impact on diagnostics, treatments, and vaccines (CDC, 2021a, 2021b; FDA, 2021; Moore and Offit, 2021; Wang et al., 2021d). Common among these six variants are mutations within the receptor binding domain (RBD) in the spike glycoprotein (S protein). The S protein protrudes from the surface of the virus and facilitates viral attachment, fusion, and entry into cells via its binding partner human angiotensin-converting enzyme 2 (ACE2) (Shang et al., 2020). Additionally, the S protein is the major target of the humoral immune response, with the majority of currently developed vaccines using this protein as their major antigenic component (Krammer, 2020). The RBD within the S protein constitutes the region against which the majority of neutralizing antibodies are directed, highlighting the importance of this region for viral infection and antibody neutralization (Barnes et al., 2020a; McCallum et al., 2021; Piccoli et al., 2020).

Mutations within the RBD of the SARS-CoV-2 S protein may confer enhanced viral fitness by increasing the affinity of the S protein for ACE2 and/or decreasing the neutralization activity of antibodies produced by the humoral response. Additionally, RBD mutations may allow increased expression or presentation of the S protein on the viral surface. Figures 1B and 1C show the S protein mutations present in each of the six variants, with the majority of common mutations found within the RBD. Additionally, three of the four VoC RBD mutations (L452R, E484K, and N501Y) are located within the receptor binding motif (RBM), which comprises the interaction interface between the S protein and ACE2. The one RBD mutation occurring outside of the RBM, K417N/T, additionally exhibits ambiguity in mutation, with the P.1 strain mutated to threonine (K417T) and the B.1.351 strain mutated to asparagine (K417N) (Figure 1B). In the present study, we aim to understand the individual and combinatorial contributions that each of these common VoC/VoI RBD mutations has on enhancing aspects of viral fitness.

Using 11 S proteins with different complements of mutations, we systematically dissect the contributions of RBD mutations toward increasing ACE2 affinity and evading neutralizing antibodies (Figure 1D) using cryoelectron microscopy (cryo-EM) structural analyses and assays that measure ACE2 and antibody

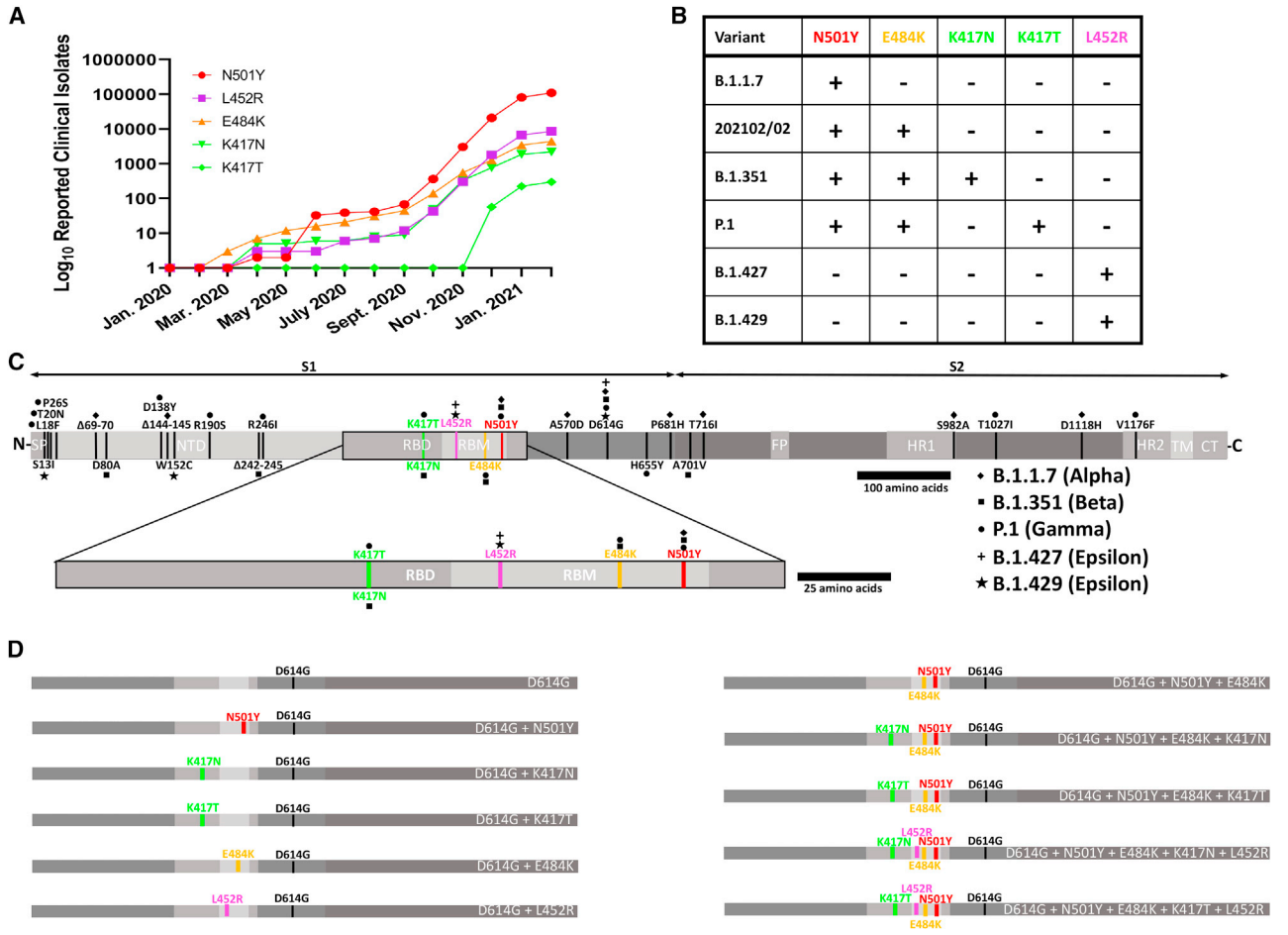

Figure 1. The global prevalence of SARS-CoV-2 VoC/VoI RBD mutations and their locations within the S protein

(A) Global occurrences of each VoC/VoI RBD mutation over time, computed using the sum of clinical isolate entries each month deposited into the GISAID database (https://www.gisaid.org/).

(B) Summary of the RBD mutations present in each variant.

(C) SARS-CoV-2 spike glycoprotein amino acid open reading frame (ORF) with variant mutations indicated. An expanded portion of the RBD is provided to highlight the common RBD mutations between the variants. Relevant features are indicated: SP, signal peptide; NTD, N-terminal domain; RBD, receptor binding domain; RBM, receptor binding motif; FP, fusion peptide; HR1, heptad repeat 1; HR2, heptad repeat 2; TM, transmembrane domain; CT, cytoplasm domain.

(D) Summary of the SARS-CoV-2 spike glycoprotein constructs used in this study. VoC/VoI RBD mutations were expressed in isolation, in naturally occurring combinations, and in novel combinations to assess the relative individual and combinatorial effects of these mutations. All constructs contain the D614G mutation as background, and this was defined as the wild-type construct throughout the study.

binding. We also constructed novel and as yet unreported combinations of RBD mutations to explore the properties of variants that may emerge in the future as the SARS-CoV-2 strains evolve.

RESULTS

The N501Y, E484K, and L452R mutations drive increased S protein-ACE2 binding affinity

To investigate the effects of VoC/VoI RBD mutations on ACE2 binding, we expressed and purified recombinant spike ectodomain proteins bearing RBD mutations in isolation and combination (Figures S1A and S1B), which we used in biolayer interferometry (BLI) experiments (Figures 2A, 2B, and S1C). Compared with wild-type (D614G), spikes harboring combinations of RBD mutations found in circulating variants exhibited increased ACE2 binding affinities. The individual addition of N501Y, E484K, or L452R mutations increased ACE2 binding affinity, and the increased affinity conferred by the N501Y and E484K mutations in isolation was preserved in combination in the D614G + N501Y + E484K construct, yielding the highest affinity ACE2 binder. Mutations at the 417 position (K417N/T) decreased the affinity for ACE2 both in isolation (D614G + K417N/T) and when introduced into the D614G + N501Y + E484K construct. Interestingly, the K417N mutation reduced ACE2 affinity to a greater extent than the K417T mutation (both in isolation and when combined with D614G + N510Y + E484K). Taken together, these results demonstrate that the amalgamation of spike RBD mutations present in circulating VoC/VoIs enables increased ACE2 affinity, which is driven mainly by N501Y (B.1.1.7), L452R (B.1.427/B.1.429), and the

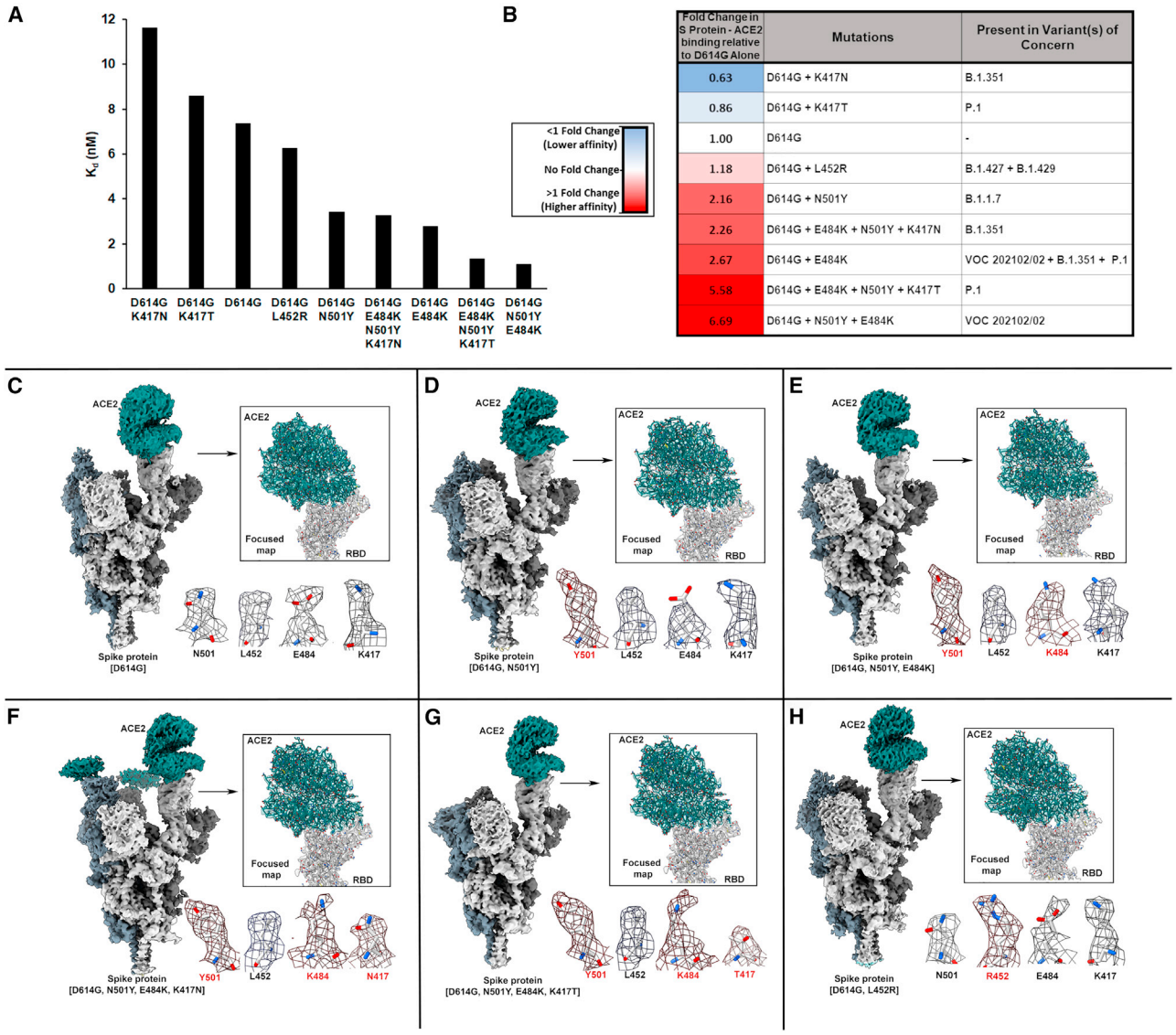

Figure 2. Complete sets of VoC/VoI RBD mutations increase S protein trimer-ACE2 binding affinity

(A) Affinity (K_d) measurements for VoC/VoI RBD mutant S protein-ACE2 binding as measured by biolayer interferometry (BLI).

(B) Relative fold change differences in S protein-ACE2 affinity (K_d) relative to D614G alone.

(C–H) Structures of VoC/VoI spike-ACE2 complexes characterized in this study. Shown for each complex studied are density maps for the overall complex at the end of global structure refinements, improved focused density maps at the ACE2-RBD contact zones, and visualization of densities at mutational positions within each variant spike. Densities at sites harboring mutations are highlighted with red text.

combinatorial effect of both N501Y and E484K (P.1, B.1.351, and VOC 202102/02).

Mutational effects on ACE2 binding are mediated by subtle side-chain rearrangements at the S protein-ACE2 interface

To understand the structural effects of the various VoC/VoI RBD mutations on ACE2 binding, we conducted cryo-EM studies on unbound spike trimers and ACE2-spike complexes (Figures 2C–2H, S2, and S3; Table S1). Resulting structures were obtained at average resolutions of ~2.3–3 Å (Figure S2; Table S1). The *apo*- and ACE2-complexed S protein structures show no significant global changes in secondary or quaternary structure as a result of the various mutations compared with D614G (Figure S4A). However, focused refinement of the S protein-ACE2 interface (Figures S3 and S4E–S4J) revealed side-chain rearrangements that may account for the observed differences in binding affinity as outlined below.

D614G + N501Y

The cryo-EM structure of ACE2 bound to the D614G + N501Y mutant spike (Figures 3B and S4C) shows the same features at the RBD-ACE2 interface as in our previously reported structure of the N501Y-ACE2 complex in the absence of the D614G mutation (Figures 3A and S4B). Y501 in the spike protein and Y41 in

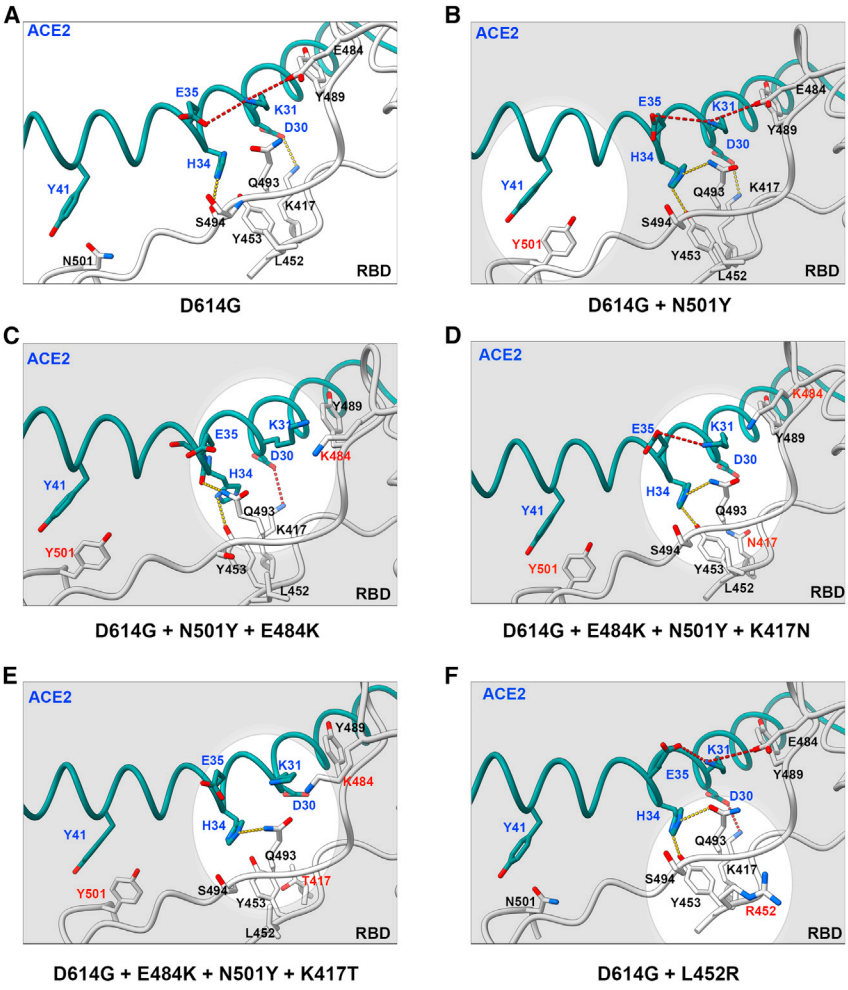

Figure 3. CryoEM structures of wild-type and VoC RBD-ACE2 interfaces

(A–F) Zoomed-in views of the RBD-ACE2 binding interfaces for the six S protein-ACE2 structures. Focused refinement of the RBD-ACE2 interface reveals distinct S protein and ACE2 side-chain rotamer arrangements for the various variants. Mutated residues are labeled in red, and adjacent residues of interest are highlighted within ovals. ACE2 residues are labeled in blue, while RBD residues are labeled in black. Hydrogen bonds and electrostatic interactions are shown as yellow and red dotted lines, respectively. Oxygen and nitrogen heteroatoms are colored in red and blue, respectively.

the ACE2 receptor engage in a perpendicularly shaped π-π stacking interaction (Zhu et al., 2021). Additionally, superposition of the RBD in all RBD-ACE2 structures reveals a ~2.4 Å displacement of an ACE2 helix distal to the RBD binding helix compared with complexes with N and Y at residue 501 reflecting the impact of this change (Figure S4D).

D614G + N501Y + E484K

Analysis of the D614G + N501Y + E484K mutant spike in complex with ACE2 reveals local rearrangements resulting in unambiguous rotamer placement of both H34 within ACE2 and Q493 within the spike RBD (Figures 3C, S4G, and S4M). The resulting H34 rotamer yields space that accommodates an alternative Q493 rotamer closer to ACE2 relative to the D614G spike, allowing it to be positioned within hydrogen-bonding distance of the main chain carbonyl of H34. Additionally, the positioning of K31 within ACE2 is shifted relative to the D614G spike, adopting a position within pi-cation bonding distance to Y489 within the RBD (Figure S4M). K484 extends parallel to the RBD-ACE2 plane of interaction, likely because of electronic repulsion from K31, and adopts a position ~7.5 Å from E35. These subtle changes in intermolecular interactions enabled upon H34 repositioning suggest a basis for the enhanced ACE2 affinity observed for the D614G + N501Y + E484K mutant spike relative to D614G + N501Y.

D614G + N501Y + E484K + K417T/N

The mutation of K417 to T or N resulted in loss of the K417-D30 salt bridge within the ACE2-spike complex, providing a basis for the decreased ACE2 binding affinities conferred by these two mutations (Figures 3D, 3E, S4N, and S4O). In contrast to the D614G + N501Y + E484K-ACE2 complex, H34 rotamer placement is ambiguous within these complexes, with the predominant densities corresponding to H34 facing toward the K484 interface. Additionally, Q493 adopts a rotamer that faces away from ACE2, and K31 is positioned to face both H34 and Q493.

D614G + L452R

Structural comparison of D614G-ACE2 and D614G + L452R-ACE2 complexes reveals no significant changes at the RBD-ACE2 interface (Figures 3F and S4P), indicating that the enhanced ACE2 affinity afforded by L452R is not due to modulation of direct ACE2 contacts. In contrast to L452, the side chain of R452 extends farther away from the RBD core (Figure S4Q) and is better exposed to solvent, suggesting that R452 may enhance the solvation of the RBD in the up position. In addition to solvation effects, the L452R substitution introduces a positive charge at position 452 that may increase the electrostatic complementarity between the RBD and ACE2. Figure S4R shows the increase in electropositivity at position 452 upon L452R substitution, with position 452 approximately 13 Å away from the highly electronegative site on ACE2 centered at E35. Thus, in contrast to the local rearrangements observed at the RBD-ACE2 interface for the N501Y, E484K, and K417N/T mutations, the binding effect of the L452R mutation is likely mediated by solvation and/or electrostatic complementarity effects.

Mutations E484K, L452R, and K417N/T facilitate decreased antibody binding

We next sought to evaluate the effect of VoC/VoI RBD mutations on antibody binding. We selected a panel of previously reported

CellPress
OPEN ACCESS

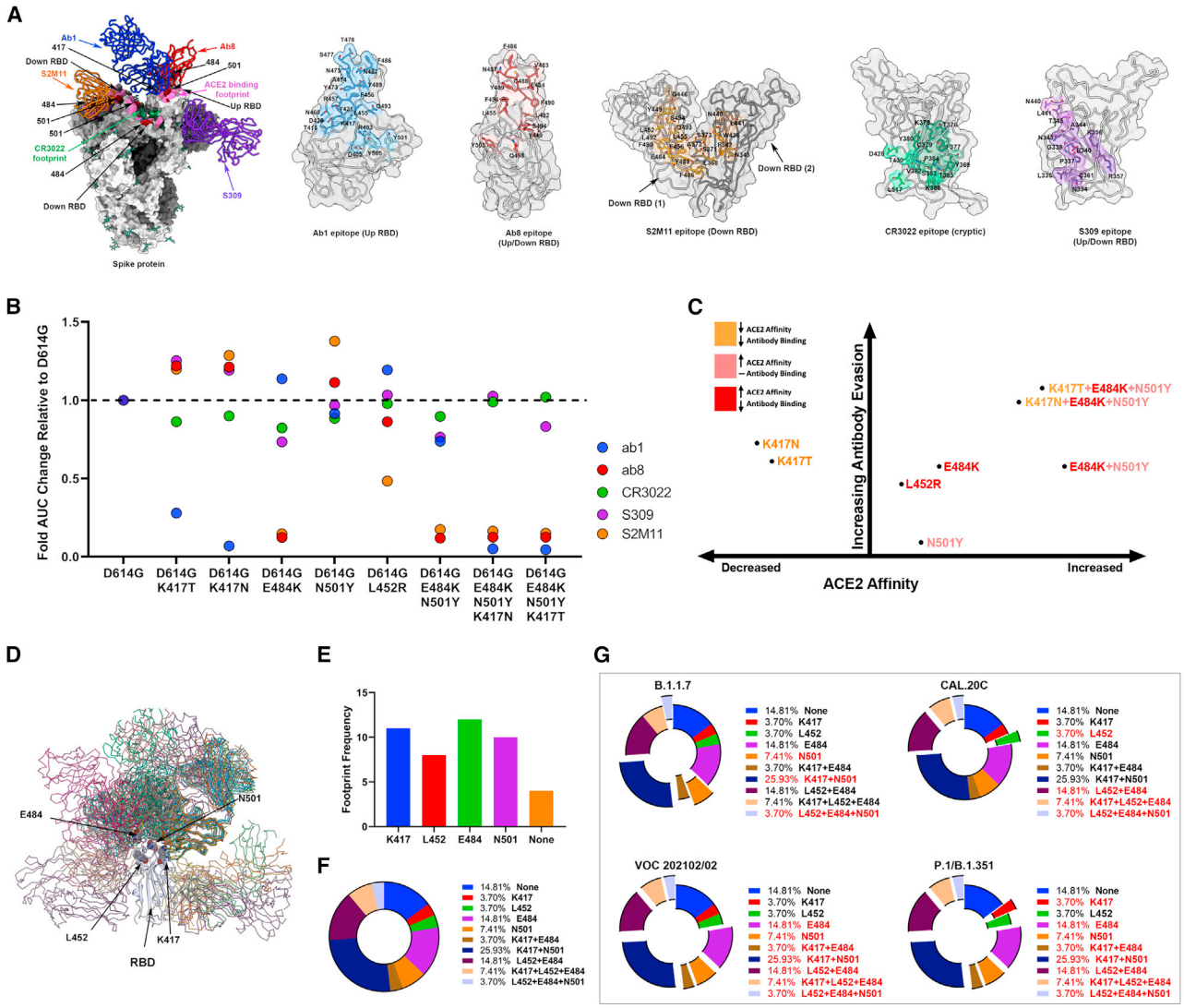

Figure 4. Monoclonal antibody binding against SARS-CoV-2 S proteins containing VoC/VoI RBD mutations

(A) Mapping of Ab1, Ab8, CR3022, S309, and S2M11 antibody footprints onto SARS-CoV-2 trimers and RBDs. Direct amino acid contacts for each individual antibody footprint are highlighted separately.

(B) Area under the curve (AUC) fold changes in ELISA binding assays relative to D614G alone for Ab1, Ab8, CR3022, S309, and S2M11.

(C) Qualitative two-dimensional (2D) plot describing VoC RBD mutational effects on ACE2 and antibody binding. The mutations are grouped into three colour categories: orange, mutations that decrease ACE2 affinity and antibody binding; pink, mutations that increase ACE2 affinity and do not significantly affect antibody binding; and red, mutations that increase ACE2 affinity and decrease antibody binding.

(D–G) PDB entries of SARS-CoV-2 spike or RBD complexes with antibody fragments isolated from convalescent patients were evaluated for the interaction with RBD positions that are mutated in VoC/VoIs. See Table S2 for PDB entries included in this analysis. (D) Structural overlap of all antibodies selected on the SARS-CoV-2 RBD. Mutational positions within the RBD are highlighted. (E) Frequency of each of the RBD positions that are mutated in VoCs within the footprints of selected antibody-spike/RBD structures. (F) Proportional analysis of distinct variant RBD positional compositions within the footprints of selected antibody-spike/RBD structures. (G) Analysis of the overlap between the mutational composition of various VoCs and distinct variant RBD positional compositions within the footprints of selected antibody-spike/RBD structures. Footprints including at least one position mutated within a given VoC are highlighted in red and depicted as slices graphically. Table S2 lists the antibodies and PDB entries selected.

antibodies that cover the four distinct anti-RBD antibody classes (Barnes et al., 2020b; Table S3) and an ultrapotent antibody, S2M11, that uniquely binds two neighboring RBDs (Tortorici et al., 2020). Antibody binding was quantified via enzyme-linked immunosorbent assay (ELISA) (Figures 4 and S1D). As expected, class 3 (S309) and class 4 (CR3022) antibodies, whose footprints did not span VoC/VoI mutations, exhibited relatively unchanged binding across all variant spikes (Figure 4B). Mutations at position 417 of the S protein to either N or T abolished or significantly reduced ab1 (Li et al., 2020a) (class 1 like) binding respectively,

demonstrating the importance of K417 within the molecular epitope of ab1. Similarly, the E484K mutation resulted in loss of binding to ab8 (Li et al., 2020b) (class 2) and S2M11, highlighting the critical nature of E484 within the epitopes of these antibodies. L452 sits peripherally within the footprint of S2M11, and mutation of this residue to R452 reduced but did not abolish its binding, possibly via steric or charge-mediated effects or by allosteric modulation of direct contacts. Taken together, these results suggest the escape of antibody binding from the four major anti-RBD classes is primarily mediated by modulation of direct contacts at mutational sites.

Novel RBD mutant combinations preserve but do not enhance effects on ACE2 affinities and antibody binding

Having determined that all full complements of VoC/VoI RBD mutations result in increased ACE2 binding and various extents of antibody evasion, we aimed to assess the functional effects of novel RBD mutational combinations that have not yet been reported but represent combinations of mutations already observed. Variants harbouring N501Y exhibit a spectrum of additional RBD mutations (B.1.1.7: N501Y; VOC 202102/02: E484K, N501Y; B.1.351: E484K, N501Y, K417N; and P.1: E484K, N501Y, K417T), while variants containing L452R (B.1.427/B.1.429) seemingly exclude N501Y, K417N/T, and E484K mutations, though there has been a recent report of E484Q co-mutation with L452R in India (B.1.617.1). In order to assess if such patterns of evolution are due to incompatibility of these mutations, we constructed and expressed recombinant spike ectodomains combining L452R with the full complement of either B.1.351 and P.1 RBD mutations and evaluated ACE2 and antibody binding of these mutants (Figures S5A–S5C). Neither of these novel combinations conferred enhanced ACE2 affinities compared with B.1.351 and P.1 RBD mutant spikes. Notably, both novel combinatorial mutants still exhibited enhanced ACE2 binding compared with wild-type (Figure S5B). The addition of L452R to both constructs preserved the antibody-evasive properties for K417N/T against ab1 and E484K against both ab8 and S2M11 (Figure S5C). These results indicate that although the L452R mutation is not mutually exclusive with the complement of RBD mutations in B.1.351 and P.1 variants with regard to reduction of neutralizing antibody binding, the increase in ACE2 binding affinity conferred by the L452R mutation in isolation (Figures 2A and 2B) is absent when combined with B.1.351 and P.1 RBD mutations.

DISCUSSION

We have dissected the relative roles of circulating VoC/VoI RBD mutations with regard to both ACE2 affinity and antibody binding (Figure 4C). Our results demonstrate that individual mutations may be classified as resulting in (1) increased RBD-ACE2 affinity (N501Y), (2) reduced ACE2 affinity and reduced antibody binding (K417N/T), or (3) a simultaneous increase in ACE2 affinity and reduced antibody binding (E484K, L452R). These individual effects are preserved when mutations are combined to reflect full complements of VoC/VoI RBD mutations, demonstrating their modular nature. Furthermore, these results suggest that RBD evolution follows a trajectory aimed at simultaneous enhancement of receptor affinity and reduction of neutralizing antibody binding. Although our analysis did not reveal the N501Y mutation to be highly antibody evasive, its presence within the footprint of several neutralizing antibodies may have implications for antibody escape (Figures 4D–4G). It is noteworthy that all VoCs containing K417N/T mutations also contain the N501Y and E484K mutations. Given that K417N/T mutations serve to diminish antibody binding at a cost to ACE2 affinity, the conditional presence of ACE2 affinity enhancing mutations may represent a compensatory mutational mechanism. Consistent with this hypothesis, analysis of deposited spike sequences in the GISAID database reveals that K417N/T mutations do not occur independently of N501Y and E484K mutations (Figure S5D). In contrast, K417N/T mutations are not a prerequisite for the occurrence of mutations that increase ACE2 affinity (N501Y) or simultaneously increase ACE2 affinity and decrease antibody binding (E484K, L452R) (Figure S5D).

Our described effects on ACE2 binding and antibody evasion imparted by VoC/VoI RBD mutations are in agreement with recent reports (Chen et al., 2021; Collier et al., 2021; Dejnirattisai et al., 2021; Laffeber et al., 2021; Liu et al., 2021; Wang et al., 2021a, 2021b; Wibmer et al., 2021; Yuan et al., 2021), with the exception of the enhanced ACE2 affinity conferred by E484K. Several studies have reported conflicting data surrounding the effect of E484K on ACE2 binding, where both decreased (Upadhyay et al., 2021; Wang et al., 2021c; Yuan et al., 2021) and increased (Laffeber et al., 2021; Tanaka et al., 2021) affinities are observed. A variety of biophysical techniques, spike protein domains, and ACE2 constructs were used across these studies, which could account for the contrasting results. Most important, the E484K mutation was among several mutations selected via *in vitro* evolution to affinity-maturate the RBD for enhanced ACE2 binding (Zahradník et al., 2021), demonstrating a clear role for increasing ACE2 binding affinity.

The present study highlights the potential for antibody evasion by VoC RBD mutations via antibody binding assays using a panel of monoclonal antibodies. To estimate the potential effect of VoC RBD mutations on RBD binding by naturally acquired antibodies during SARS-CoV-2 infection, we selected PDB entries of SARS-CoV-2 spike or RBD complexes with antibody fragments isolated from convalescent patients (Table S2). Using these structural data, we evaluated the frequency of positions corresponding to RBD mutations in VoC/VoIs within the footprint of 27 selected antibodies (Banach et al., 2021; Barnes et al., 2020a, 2020b; Cao et al., 2020; Hurlburt et al., 2020; Ju et al., 2020; Kim et al., 2021; Liu et al., 2020; Piccoli et al., 2020; Shi et al., 2020; Wu et al., 2020a, 2020b; Yuan et al., 2020; Zhou et al., 2020). The majority of deposited human-derived neutralizing antibodies bound the RBD with footprints spanning at least one of the positions corresponding to RBD mutation in VoC/VoIs (Figure 4E). Of these antibodies, the majority interacted with more than one position corresponding to RBD mutations in VoC/VoIs (Figure 4F). Of these variants, B.1.351, P.1, and VOC 202102/02 possess mutations that are collectively recognized by the majority of the antibodies selected, suggesting that these variants may exhibit the greatest RBD-directed antibody escape during human infection (Figure 4G).

We additionally generated novel combinations of RBD mutations by introducing L452R into B.1.351 and P.1 constructs. Although these mutational combinations enable enhanced ACE2 binding compared with wild-type spikes, the increase in ACE2 binding affinity conferred by the L452R mutation in isolation was not preserved. We demonstrate that these novel constructs retain antibody-evasive properties when tested for antibody binding using a panel of monoclonal antibodies. Although there are many factors governing viral evolution, these results suggest that the independent evolution of L452R-bearing spikes and N501Y-, K417N/T-, and E484K-bearing spikes may be explained by a lack of synergistic increase in ACE2 binding upon combination of these mutations. Such combinations may however still evolve in the future as a result of increased antibody escape.

The cryo-EM structures of all five VoC/VoI RBD-mutated spike trimers, both in isolation and in complex with ACE2, provide insights regarding the molecular basis for observed changes in ACE2 affinities. The combination of enhanced intermolecular interactions due to the concomitant repositioning of H34 and Q493 in the D614G + N501Y + E484K-ACE2 complex provides structural rationale for the increased ACE2 binding affinity relative to the D614G + N501Y spike. Although hydrogen bonding with Y453 is possible in both H34 rotamers (Figures S4K–S4P), the dominant rotamer positioning of H34 in the D614G + N501Y + E484K-ACE2 complex enables it to participate in additional favourable intermolecular interactions with Y453 (hydrogen bond + OH/π) and L455 (CH/π), yielding estimated interaction energies of -10.29 and -2.75 kcal/mol, respectively (Watanabe et al., 2021). The mechanism of H34 rotamer stabilization in response to the E484K mutation remains unclear at present, although the repositioning of Q493 in this structure permits the formation of an intermolecular hydrogen bond with the main chain carbonyl of H34. This is in contrast to all other structures of spike protein-ACE2 complexes in which Q493 is positioned in close proximity to the main chain RBD carbonyls of F490 and L492 and is well poised to participate in intramolecular hydrogen bonds (Figures S4K–S4P). Finally, the positioning of K31 within pi-cation bonding distance to Y489 in this structure suggests an additional intermolecular interaction that may enhance ACE2 affinity (Figure S4M). It should be noted that although the intermolecular K31-E484 salt bridge is lost upon inclusion of the E484K mutation, this electrostatic interaction is likely intramolecularly distributed between ACE2 residues E35 and K31, thus limiting the contribution of the K31-E484 interaction with regard to ACE2-RBD binding. The positioning of H34 away from residue 484 in all RBD-ACE2 crystal structures reported (PDB: 6M0J, PDB: 6VW1, and PDB: 7NXC) agrees with our assessment that this represents the more energetically favourable rotamer with regard to the stability of the RBD-ACE2 complex. This structural basis is consistent with previous reports implicating H34 as a major contributor to the SARS-CoV-2 RBD-ACE2 interaction (Glasgow et al., 2020) and reports demonstrating the H34A mutation in ACE2 enhances SARS-CoV-2 spike binding (Chan et al., 2020; Tanaka et al., 2021). This is likely due to closer positioning and flexibility of RBD residues such as Q493. Recent reports have suggested that the E484K mutation may enhance ACE2 binding via increasing electrostatic complementarity between ACE2 and the RBD (Dejnirattisai et al., 2021; Fantini et al., 2021), and the structures reported here are consistent with that hypothesis. The combination of the L452R mutation with either Beta or Gamma variant RBD mutations (D614G + N501Y + E484K + K417N/T) did not further increase ACE2 affinity. This may be explained by electrostatic complementarity effects; namely, E484K already introduces complementary electropositivity near the electronegative site on ACE2 (centered at residues E35 and K31), so the addition of further electropositivity at the more distal L452 position (by the addition of L452R) likely does not additionally enhance the S protein-ACE2 electrostatic complementarity. The structural basis for the observed discrepancies in ACE2 binding between the K417T and K417N mutations remains unclear.

As L452 is distal to the ACE2-RBD interface, it has been previously suggested that the L452R mutation may increase ACE2 affinity via allosteric modulation of the residues promoting the RBD-ACE2 interaction (Deng et al., 2021) or via electrostatic effects (Motozono et al., 2021). We did not observe any allosteric changes in our structures; rather we highlight the enhanced RBD-ACE2 electrostatic complementarity and potentially increased RBD solvation as explanations for the increased ACE2 affinity conferred by R452. Protein-protein interaction studies have predicted that long-range electrostatic complementarity plays a role in determining complex association rates (Schreiber et al., 2009). Therefore, the increased electrostatic complementarity between ACE2 and the RBD due to R452 may enhance ACE2 affinity by increasing the probability of forming favourable RBD-ACE2 binding orientations. The increased solvation and electrostatic complementarity explanations are not mutually exclusive and may contribute to increased ACE2 affinity in combination.

Limitations of the study

We have assessed VoC RBD mutations for their impact on ACE2 and antibody binding, two important but not comprehensive readouts on viral fitness (protein stability and RBD up/down propensity are other aspects of viral fitness not assessed here). Our analyses make use of trimeric HexaPro-stabilized S protein ectodomain constructs, which differ from native S protein trimers by the addition of six stabilizing proline mutations (F817P, A892P, A899P, A942P, K968P, and V969P) and the transmembrane domain replaced with a trimerization motif (Hsieh et al., 2020). The HexaPro construct produces substantially higher yields in mammalian cell culture and has increased thermostability, which facilitates the structural and biochemical experiments presented here. The S protein-ACE2 BLI study presented here produced modest (0.63–6.69) fold changes in binding for the RBD mutants relative to wild-type (D614G) S protein and may not reflect absolute quantitative changes within the context of live virus infections. Although we have focused the present study on RBD mutations present within VoCs, it has been demonstrated that mutations elsewhere in the S protein (particularly in the N-terminal domain) also play a significant role in antibody evasion and may affect ACE2 binding (McCallum et al., 2021). Mutations outside of the S protein open reading frame may additionally contribute to increased viral fitness. Future studies will likely provide further insights into these aspects of SARS-CoV-2 infection and global spread.

STAR★METHODS

Detailed methods are provided in the online version of this paper and include the following:

- KEY RESOURCES TABLE
- RESOURCE AVAILABILITY
  - Lead contact
  - Materials availability
  - Data and code availability
- EXPERIMENTAL MODEL AND SUBJECT DETAILS
- METHOD DETAILS
  - Cloning, expression and purification of recombinant spike protein constructs
  - Antibody production
  - Electron microscopy sample preparation and data collection
  - Image processing
  - Model building and refinement
  - Biolayer interferometry (BLI) S protein-ACE2 binding assay
  - Enzyme-linked immunosorbent assay (ELISA)
  - Analysis of convalescent patient antibody footprints
- QUANTIFICATION AND STATISTICAL ANALYSIS

SUPPLEMENTAL INFORMATION

Supplemental information can be found online at https://doi.org/10.1016/j.celrep.2021.110156.

ACKNOWLEDGMENTS

This work was supported by awards to S.S. from a Canada Excellence Research Chair Award, the VGH Foundation, and Genome BC, Canada, and a generous donation from the Tai Hung Fai Charitable Foundation. W.L. and D.S.D. were supported by the University of Pittsburgh Medical Center. D.M. is supported by a CIHR Frederick Banting and Charles Best Canada Graduate Scholarship Master's Award (CGS-M). J.W.S. is supported by a CIHR Frederick Banting and Charles Best Canada Graduate Scholarships Doctoral Award (CGS-D) and a UBC President's Academic Excellence Initiative PhD Award. We thank Sagar Chittori for assistance with microscopy screening and collection.

AUTHOR CONTRIBUTIONS

J.W.S. and D.M. performed the molecular cloning. J.W.S., D.M., S.Z., and S.S.S. carried out expression and purification of the spike proteins and antibody fragments. A.K. performed the BLI binding assays under the supervision of W.L. and D.S.D. D.M. and J.W.S. performed the antibody binding experiments. A.M.B. and K.S.T. collectively carried out the experimental components of cryo-EM and electron microscopy including specimen preparation and data collection. X.Z. carried out all computational aspects of image processing and structure determination. D.M., X.Z., S.S.S., and S.S. interpreted and analyzed the cryo-EM structures. A.K., W.L., and D.S.D. provided the plasmids for VH-ab8 and IgG ab1 as part of a collaboration between the Subramaniam and Dimitrov laboratories on SARS-CoV-2. D.M., J.W.S., S.S.S., and S.S. drafted the initial manuscript with input from all authors.

DECLARATION OF INTERESTS

W.L. and D.S.D. are coinventors on a patent, filed by the University of Pittsburgh, related to ab1 and ab8 described in this paper. S.S. is founder and CEO of Gandeeva Therapeutics Inc.

Received: July 15, 2021
Revised: October 20, 2021
Accepted: December 1, 2021
Published: December 4, 2021

REFERENCES

Afonine, P.V., Poon, B.K., Read, R.J., Sobolev, O.V., Terwilliger, T.C., Urzhumtsev, A., and Adams, P.D. (2018). Real-space refinement in PHENIX for cryo-EM and crystallography. Acta Crystallogr. D Struct. Biol. *74*, 531–544.

Banach, B.B., Cerutti, G., Fahad, A.S., Shen, C.-H., de Souza, M.O., Katsamba, P.S., Tsybovsky, Y., Wang, P., Nair, M.S., Huang, Y., et al. (2021). Paired heavy and light chain signatures contribute to potent SARS-CoV-2 neutralization in public antibody responses. bioRxiv. https://doi.org/10.1101/2020.12.31.424987.

Barnes, C.O., West, A.P.J., Huey-Tubman, K.E., Hoffmann, M.A.G., Sharaf, N.G., Hoffman, P.R., Koranda, N., Gristick, H.B., Gaebler, C., Muecksch, F., et al. (2020a). Structures of human antibodies bound to SARS-CoV-2 spike reveal common epitopes and recurrent features of antibodies. Cell *182*, 828–842.e16.

Barnes, C.O., Jette, C.A., Abernathy, M.E., Dam, K.-M.A., Esswein, S.R., Gristick, H.B., Malyutin, A.G., Sharaf, N.G., Huey-Tubman, K.E., Lee, Y.E., et al. (2020b). SARS-CoV-2 neutralizing antibody structures inform therapeutic strategies. Nature *588*, 682–687.

Bell, J.M., Chen, M., Baldwin, P.R., and Ludtke, S.J. (2016). High resolution single particle refinement in EMAN2.1. Methods *100*, 25–34.

Cao, Y., Su, B., Guo, X., Sun, W., Deng, Y., Bao, L., Zhu, Q., Zhang, X., Zheng, Y., Geng, C., et al. (2020). Potent neutralizing antibodies against SARS-CoV-2 identified by high-throughput single-cell sequencing of convalescent patients' B cells. Cell *182*, 73–84.e16.

CDC (2021a). SARS-CoV-2 Variant Classifications and Definitions (CDC).

CDC (2021b). Science Brief: Emerging SARS-CoV-2 Variants (CDC).

Chan, K.K., Dorosky, D., Sharma, P., Abbasi, S.A., Dye, J.M., Kranz, D.M., Herbert, A.S., and Procko, E. (2020). Engineering human ACE2 to optimize binding to the spike protein of SARS coronavirus 2. Science *369*, 1261–1265.

Chen, V.B., Arendall, W.B., 3rd, Headd, J.J., Keedy, D.A., Immormino, R.M., Kapral, G.J., Murray, L.W., Richardson, J.S., and Richardson, D.C. (2010). MolProbity: all-atom structure validation for macromolecular crystallography. Acta Crystallogr. D Biol. Crystallogr. *66*, 12–21.

Chen, R.E., Zhang, X., Case, J.B., Winkler, E.S., Liu, Y., VanBlargan, L.A., Liu, J., Errico, J.M., Xie, X., Suryadevara, N., et al. (2021). Resistance of SARS-CoV-2 variants to neutralization by monoclonal and serum-derived polyclonal antibodies. Nat. Med. *27*, 717–726.

Collier, D.A., De Marco, A., Ferreira, I.A.T.M., Meng, B., Datir, R.P., Walls, A.C., Kemp, S.A., Bassi, J., Pinto, D., Silacci-Fregni, C., et al. (2021). Sensitivity of SARS-CoV-2 B.1.1.7 to mRNA vaccine-elicited antibodies. Nature *593*, 136–141.

Dejnirattisai, W., Zhou, D., Supasa, P., Liu, C., Mentzer, A.J., Ginn, H.M., Zhao, Y., Duyvesteyn, H.M.E., Tuekprakhon, A., Nutalai, R., et al. (2021). Antibody evasion by the P.1 strain of SARS-CoV-2. Cell *184*, 2939–2954.e9.

Deng, X., Garcia-Knight, M.A., Khalid, M.M., Servellita, V., Wang, C., Morris, M.K., Sotomayor-González, A., Glasner, D.R., Reyes, K.R., Gliwa, A.S., et al. (2021). Transmission, infectivity, and neutralization of a spike L452R SARS-CoV-2 variant. Cell *184*, 3426–3437.e8.

Emsley, P., Lohkamp, B., Scott, W.G., and Cowtan, K. (2010). Features and development of coot. Acta Crystallogr. D. Biol. Crystallogr. *66*, 486–501.

Fantini, J., Yahi, N., Azzaz, F., and Chahinian, H. (2021). Structural dynamics of SARS-CoV-2 variants: a health monitoring strategy for anticipating Covid-19 outbreaks. J. Infect. https://doi.org/10.1016/j.jinf.2021.06.001.

FDA (2021). Genetic Variants of SARS-CoV-2 May Lead to False Negative Results with Molecular Tests for Detection of SARS-CoV-2 - Letter to Clinical Laboratory Staff and Health Care Providers (FDA).

Glasgow, A., Glasgow, J., Limonta, D., Solomon, P., Lui, I., Zhang, Y., Nix, M.A., Rettko, N.J., Zha, S., Yamin, R., et al. (2020). Engineered ACE2 receptor traps potently neutralize SARS-CoV-2. Proc. Natl. Acad. Sci. U S A *117*, 28046–28055.

Goddard, T.D., Huang, C.C., Meng, E.C., Pettersen, E.F., Couch, G.S., Morris, J.H., and Ferrin, T.E. (2018). UCSF ChimeraX: meeting modern challenges in visualization and analysis. Protein Sci. *27*, 14–25.

Hsieh, C.-L., Goldsmith, J.A., Schaub, J.M., DiVenere, A.M., Kuo, H.-C., Javanmardi, K., Le, K.C., Wrapp, D., Lee, A.G., Liu, Y., et al. (2020). Structure-based design of prefusion-stabilized SARS-CoV-2 spikes. Science *369*, 1501–1505.

Hurlburt, N.K., Seydoux, E., Wan, Y.-H., Edara, V.V., Stuart, A.B., Feng, J., Suthar, M.S., McGuire, A.T., Stamatatos, L., and Pancera, M. (2020). Structural basis for potent neutralization of SARS-CoV-2 and role of antibody affinity maturation. Nat. Commun. *11*, 5413.

Ju, B., Zhang, Q., Ge, J., Wang, R., Sun, J., Ge, X., Yu, J., Shan, S., Zhou, B., Song, S., et al. (2020). Human neutralizing antibodies elicited by SARS-CoV-2 infection. Nature *584*, 115–119.

Kim, C., Ryu, D.-K., Lee, J., Kim, Y.-I., Seo, J.-M., Kim, Y.-G., Jeong, J.-H., Kim, M., Kim, J.-I., Kim, P., et al. (2021). A therapeutic neutralizing antibody targeting receptor binding domain of SARS-CoV-2 spike protein. Nat. Commun. *12*, 288.

Krammer, F. (2020). SARS-CoV-2 vaccines in development. Nature *586*, 516–527.

Laffeber, C., de Koning, K., Kanaar, R., and Lebbink, J.H.G. (2021). Experimental evidence for enhanced receptor binding by rapidly spreading SARS-CoV-2 variants. J. Mol. Biol. *433*, 167058.

Laskowski, R.A., Jabłońska, J., Pravda, L., Vařeková, R.S., and Thornton, J.M. (2018). PDBsum: structural summaries of PDB entries. Protein Sci. *27*, 129–134.

Li, W., Chen, C., Drelich, A., Martinez, D.R., Gralinski, L.E., Sun, Z., Schäfer, A., Kulkarni, S.S., Liu, X., Leist, S.R., et al. (2020a). Rapid identification of a human antibody with high prophylactic and therapeutic efficacy in three animal models of SARS-CoV-2 infection. Proc. Natl. Acad. Sci. U S A *117*, 29832–29838.

Li, W., Schäfer, A., Kulkarni, S.S., Liu, X., Martinez, D.R., Chen, C., Sun, Z., Leist, S.R., Drelich, A., Zhang, L., et al. (2020b). High potency of a bivalent human V(H) domain in SARS-CoV-2 animal models. Cell *183*, 429–441.e16.

Liu, L., Wang, P., Nair, M.S., Yu, J., Rapp, M., Wang, Q., Luo, Y., Chan, J.F.-W., Sahi, V., Figueroa, A., et al. (2020). Potent neutralizing antibodies against multiple epitopes on SARS-CoV-2 spike. Nature *584*, 450–456.

Liu, Z., VanBlargan, L.A., Bloyet, L.-M., Rothlauf, P.W., Chen, R.E., Stumpf, S., Zhao, H., Errico, J.M., Theel, E.S., Liebeskind, M.J., et al. (2021). Identification of SARS-CoV-2 spike mutations that attenuate monoclonal and serum antibody neutralization. Cell Host Microbe *29*, 477–488.e4.

McCallum, M., De Marco, A., Lempp, F.A., Tortorici, M.A., Pinto, D., Walls, A.C., Beltramello, M., Chen, A., Liu, Z., Zatta, F., et al. (2021). N-terminal domain antigenic mapping reveals a site of vulnerability for SARS-CoV-2. Cell *184*, 2332–2347.e16.

Moore, J.P., and Offit, P.A. (2021). SARS-CoV-2 vaccines and the growing threat of viral variants. JAMA *325*, 821–822.

Motozono, C., Toyoda, M., Zahradnik, J., Ikeda, T., Saito, A., Tan, T.S., Ngare, I., Nasser, H., Kimura, I., Uriu, K., et al. (2021). An emerging SARS-CoV-2 mutant evading cellular immunity and increasing viral infectivity. bioRxiv. https://doi.org/10.1101/2021.04.02.438288.

Pettersen, E.F., Goddard, T.D., Huang, C.C., Couch, G.S., Greenblatt, D.M., Meng, E.C., and Ferrin, T.E. (2004). UCSF Chimera–a visualization system for exploratory research and analysis. J. Comput. Chem. *25*, 1605–1612.

Piccoli, L., Park, Y.-J., Tortorici, M.A., Czudnochowski, N., Walls, A.C., Beltramello, M., Silacci-Fregni, C., Pinto, D., Rosen, L.E., Bowen, J.E., et al. (2020). Mapping neutralizing and immunodominant sites on the SARS-CoV-2 spike receptor-binding domain by structure-guided high-resolution serology. Cell *183*, 1024–1042.e21.

Pinto, D., Park, Y.-J., Beltramello, M., Walls, A.C., Tortorici, M.A., Bianchi, S., Jaconi, S., Culap, K., Zatta, F., De Marco, A., et al. (2020). Cross-neutralization of SARS-CoV-2 by a human monoclonal SARS-CoV antibody. Nature *583*, 290–295. https://doi.org/10.1038/s41586-020-2349-y.

Punjani, A., Rubinstein, J.L., Fleet, D.J., and Brubaker, M.A. (2017). cryoSPARC: algorithms for rapid unsupervised cryo-EM structure determination. Nat. Methods *14*, 290–296.

Scheres, S.H.W. (2012). A Bayesian view on cryo-EM structure determination. J. Mol. Biol. *415*, 406–418. https://doi.org/10.1016/j.jmb.2011.11.010.

Schreiber, G., Haran, G., and Zhou, H.-X. (2009). Fundamental aspects of Protein−Protein association kinetics. Chem. Rev. *109*, 839–860.

Shang, J., Wan, Y., Luo, C., Ye, G., Geng, Q., Auerbach, A., and Li, F. (2020). Cell entry mechanisms of SARS-CoV-2. Proc. Natl. Acad. Sci. U S A *117*, 11727–11734.

Shi, R., Shan, C., Duan, X., Chen, Z., Liu, P., Song, J., Song, T., Bi, X., Han, C., Wu, L., et al. (2020). A human neutralizing antibody targets the receptor-binding site of SARS-CoV-2. Nature *584*, 120–124.

Tanaka, S., Nelson, G., Olson, A., Buzko, O., Higashide, W., Shin, A., Gonzales, M., Taft, J., Patel, R., Buta, S., et al. (2021). A recombinant 'ACE2 Triple Decoy' that traps and neutralizes SARS-CoV-2 shows enhanced affinity for highly transmissible SARS-CoV-2 variants. bioRxiv. https://doi.org/10.1101/2021.03.09.434641.

Tortorici, M.A., Beltramello, M., Lempp, F.A., Pinto, D., Dang, H.V., Rosen, L.E., McCallum, M., Bowen, J., Minola, A., Jaconi, S., et al. (2020). Ultrapotent human antibodies protect against SARS-CoV-2 challenge via multiple mechanisms. Science *370*, 950–957.

Upadhyay, V., Lucas, A., Panja, S., and Mallela, K.M.G. (2021). Interplay between protein stability, binding to ACE2 and escape from neutralizing antibodies determines the natural selection of SARS-CoV-2 receptor binding domain variants. bioRxiv. https://doi.org/10.1101/2021.05.23.445348.

Wang, P., Nair, M.S., Liu, L., Iketani, S., Luo, Y., Guo, Y., Wang, M., Yu, J., Zhang, B., Kwong, P.D., et al. (2021a). Antibody resistance of SARS-CoV-2 variants B.1.351 and B.1.1.7. Nature *593*, 130–135.

Wagner, T., Merino, F., Stabrin, M., Moriya, T., Antoni, C., Apelbaum, A., Hagel, P., Sitsel, O., Raisch, T., Prumbaum, D., et al. (2019). SPHIRE-crYOLO is a fast and accurate fully automated particle picker for cryo-EM. Commun. Biol. *2*, 218. https://doi.org/10.1038/s42003-019-0437-z.

Wang, P., Casner, R.G., Nair, M.S., Wang, M., Yu, J., Cerutti, G., Liu, L., Kwong, P.D., Huang, Y., Shapiro, L., et al. (2021b). Increased resistance of SARS-CoV-2 variant P.1 to antibody neutralization. Cell Host Microbe *29*, 747–751.e4.

Wang, R., Zhang, Q., Ge, J., Ren, W., Zhang, R., Lan, J., Ju, B., Su, B., Yu, F., Chen, P., et al. (2021c). Analysis of SARS-CoV-2 variant mutations reveals neutralization escape mechanisms and the ability to use ACE2 receptors from additional species. Immunity *54*, 1611–1621.e5.

Wang, Z., Schmidt, F., Weisblum, Y., Muecksch, F., Barnes, C.O., Finkin, S., Schaefer-Babajew, D., Cipolla, M., Gaebler, C., Lieberman, J.A., et al. (2021d). mRNA vaccine-elicited antibodies to SARS-CoV-2 and circulating variants. Nature *592*, 616–622.

Watanabe, C., Okiyama, Y., Tanaka, S., Fukuzawa, K., and Honma, T. (2021). Molecular recognition of SARS-CoV-2 spike glycoprotein: quantum chemical hot spot and epitope analyses. Chem. Sci. *12*, 4722–4739.

Wibmer, C.K., Ayres, F., Hermanus, T., Madzivhandila, M., Kgagudi, P., Oosthuysen, B., Lambson, B.E., de Oliveira, T., Vermeulen, M., van der Berg, K., et al. (2021). SARS-CoV-2 501Y.V2 escapes neutralization by South African COVID-19 donor plasma. Nat. Med. *27*, 622–625.

Wu, N.C., Yuan, M., Liu, H., Lee, C.-C.D., Zhu, X., Bangaru, S., Torres, J.L., Caniels, T.G., Brouwer, P.J.M., van Gils, M.J., et al. (2020a). An alternative binding mode of IGHV3-53 antibodies to the SARS-CoV-2 receptor binding domain. Cell Rep. *33*, 108274.

Wu, Y., Wang, F., Shen, C., Peng, W., Li, D., Zhao, C., Li, Z., Li, S., Bi, Y., Yang, Y., et al. (2020b). A noncompeting pair of human neutralizing antibodies block COVID-19 virus binding to its receptor ACE2. Science *368*, 1274–1278.

Yuan, M., Liu, H., Wu, N.C., Lee, C.-C.D., Zhu, X., Zhao, F., Huang, D., Yu, W., Hua, Y., Tien, H., et al. (2020). Structural basis of a shared antibody response to SARS-CoV-2. Science *369*, 1119–1123.

Yuan, M., Huang, D., Lee, C.-C.D., Wu, N.C., Jackson, A.M., Zhu, X., Liu, H., Peng, L., van Gils, M.J., Sanders, R.W., et al. (2021). Structural and functional ramifications of antigenic drift in recent SARS-CoV-2 variants. Science *373*, eabh1139.

Zahradník, J., Marciano, S., Shemesh, M., Zoler, E., Chiaravalli, J., Meyer, B., Rudich, Y., Dym, O., Elad, N., and Schreiber, G. (2021). SARS-CoV-2 RBD in vitro evolution follows contagious mutation spread, yet generates an able infection inhibitor. bioRxiv. https://doi.org/10.1101/2021.01.06.425392.

Zhou, D., Duyvesteyn, H.M.E., Chen, C.-P., Huang, C.-G., Chen, T.-H., Shih, S.-R., Lin, Y.-C., Cheng, C.-Y., Cheng, S.-H., Huang, Y.-C., et al. (2020). Structural basis for the neutralization of SARS-CoV-2 by an antibody from a convalescent patient. Nat. Struct. Mol. Biol. *27*, 950–958.

Zhu, X., Mannar, D., Srivastava, S.S., Berezuk, A.M., Demers, J.-P., Saville, J.W., Leopold, K., Li, W., Dimitrov, D.S., Tuttle, K.S., et al. (2021). Cryo-electron microscopy structures of the N501Y SARS-CoV-2 spike protein in complex with ACE2 and 2 potent neutralizing antibodies. PLoS Biol. *19*, e3001237.

STAR★METHODS

KEY RESOURCES TABLE

REAGENT or RESOURCE	SOURCE	IDENTIFIER
Antibodies		
VH ab8	(Li et al., 2020a)	N/A
IgG1 ab1	(Li et al., 2020b)	N/A
IgG1 CR3022	(Yuan et al., 2020)	N/A
Fab S309	(Pinto et al., 2020)	N/A
Fab S2M11	(Tortorici et al., 2020)	N/A
goat anti human IgG	Jackson ImmunoReserach	Cat. # 109-035-088
Chemicals, peptides, and recombinant proteins		
Ace2 (18-615)	New England Biolabs	Cat. # 73775S
Linear Polyethylenimine	Polysciences	Cat# 23966-1
Critical commercial assays		
Pierce 1-Step Ultra Substrate Solution	ThermoFisher	Cat. # 34028
Q5 Site-Directed mutagenesis kit	NEB	Cat. # E0554S
Experimental models: Cell lines		
Expi293F	ThermoFisher	Cat# A14527
Recombinant DNA		
pαH SARS-CoV-2 S HexaPro	(Hsieh et al., 2020)	Addgene #154754
pαH HexaPro D614G	This paper	N/A
pαH HexaPro D614G + N501Y	This paper	N/A
pαH HexaPro D614G + K417N	This paper	N/A
pαH HexaPro D614G + K417T	This paper	N/A
pαH HexaPro D614G + E484K	This paper	N/A
pαH HexaPro D614G + L452R	This paper	N/A
pαH HexaPro D614G + N501Y + E484K	This paper	N/A
pαH HexaPro D614G + N501Y + E484K + K417N	This paper	N/A
pαH HexaPro D614G + N501Y + E484K + K417T	This paper	N/A
pαH HexaPro D614G + N501Y + E484K + K417N + L452R	This paper	N/A
pαH HexaPro D614G + N501Y + E484K + K417T + L452R	This paper	N/A
pcDNA3.1 Fab S309 Light Chain	This paper	N/A
pcDNA3.1 Fab S309 Heavy Chain	This paper	N/A
pcDNA3.1 Fab S2M11 Light Chain	This paper	N/A
pcDNA3.1 Fab S2M11 Heavy Chain	This paper	N/A
Software and algorithms		
GraphPad Prism	GraphPad 7.0	https://www.graphpad.com/scientific-software/prism/
EPU automated acquisition	ThermoFisher Scientific	https://www.thermofisher.com/us/en/home/electron-microscopy/products/software-em-3d-vis/epu-software.html
UCSF Chimera	(Pettersen et al., 2004)	https://www.cgl.ucsf.edu/chimera/
RELION 3.1	(Scheres, 2012)	https://github.com/3dem/relion/releases/tag/3.1.0
crYOLO (version 1.7.4)	(Wagner et al., 2019)	https://pypi.org/project/cryolo/
cryoSPARC live (v3.0.1)	(Punjani et al., 2017)	https://cryosparc.com/live

(*Continued on next page*)

Continued

REAGENT or RESOURCE	SOURCE	IDENTIFIER
Deposited data		
S(D614G)	This Paper	EMDB: 25503, PDB: 7SXR
S(D614G)+ACE2	This Paper	global refinement: EMDB: 25509, PDB: 7SXX, focus refinement: EMDB: 25510, PDB: 7SXY
S(D614G,L452R)	This Paper	EMDB: 25504; PDB: 7SXS
S(D614G,L452R) + ACE2	This Paper	global refinement: EMDB: 25511; PDB: 7SXZ, focus refinement: EMDB: 25512; PDB: 7SY0
S(D614G,N501Y)	This Paper	EMDB: 25505; PDB: 7SXT
S(D614G,N501Y) + ACE2	This Paper	global refinement: EMDB: 25513; PDB: 7SY1, focus refinement: EMDB: 25514; PDB: 7SY2
S(D614G,N501Y,E484K)	This Paper	EMDB: 25506; PDB: 7SXU
S(D614G,N501Y,E484K) + ACE2	This Paper	global refinement: EMDB: 25515; PDB: 7SY3, focus refinement: EMDB: 25516; PDB: 7SY4
S(D614G,N501Y,E484K,K417N)	This Paper	EMDB: 25507, PDB: 7SXV
S(D614G,N501Y,E484K,K417N) + ACE2	This Paper	global refinement: EMDB: 25517; PDB: 7SY5, focus refinement: EMDB: 25518; PDB: 7SY6
S(D614G,N501Y,E484K,K417T)	This Paper	EMDB: 25508; PDB: 7SXW
S(D614G,N501Y,E484K,K417T) + ACE2	This Paper	global refinement: EMDB: 25519; PDB: 7SY7, focus refinement: EMDB: 25520; PDB: 7SY8

RESOURCE AVAILABILITY

Lead contact

Further information and requests for resources and reagents should be directed to and will be fulfilled by the Lead Contact, Sriram Subramaniam (Sriram.Subramaniam@ubc.ca).

Materials availability

All unique/stable reagents generated in this study are available from the Lead Contact with a completed Materials Transfer Agreement.

Data and code availability

- Cryo-EM reconstructions and atomic models generated during this study are available at the PDB and EMBD databases (https://www.rcsb.org; http://emsearch.rutgers.edu) under the following accession codes: (Cryo-EM maps: EMDB: 25503, EMDB: 25509, EMDB: 25510, EMDB: 25504, EMDB: 25511, EMDB: 25512, EMDB: 25505, EMDB: 25513, EMDB: 25514, EMDB: 25506, EMDB: 25515, EMDB: 25516, EMDB: 25507, EMDB: 25517, EMDB: 25518, EMDB: 25508, EMDB ;25519, EMDB: 25520), (Atomic coordinate models: PDB: 7SXR, PDB: 7SXX, PDB: 7SXY, PDB: 7SXS, PDB: 7SXZ, PDB: 7SY0, PDB: 7SXT, PDB: 7SY1, PDB: 7SY2, PDB: 7SXU, PDB: 7SY3, PDB: 7SY4, PDB: 7SXV, PDB: 7SY5, PDB: 7SY6, PDB: 7SXW, PDB: 7SY7, PDB: 7SY8).
- This paper does not report original code.
- Any additional information required to reanalyze the data reported in this paper is available from the lead contact upon request.

EXPERIMENTAL MODEL AND SUBJECT DETAILS

Expi293F cells (ThermoFisher, Cat# A14527) were grown in suspension culture using Expi293 Expression Medium (ThermoFisher, Cat# A1435102) at 37°C, 8% CO2 with agitation at 130 rpm.

METHOD DETAILS

Cloning, expression and purification of recombinant spike protein constructs

The wild type SARS-CoV-2 S HexaPro expression plasmid was previously described (Hsieh et al., 2020) and was a gift from Jason McLellan (Addgene plasmid #154754; http://n2t.net/addgene:154754; RRID:Addgene_154754).

The VoC RBD mutations were introduced by site-directed mutagenesis (Q5 Site-Directed Mutagenesis Kit, New England Biolabs). Successful cloning was confirmed by Sanger sequencing (Genewiz, Inc.).

Expi293 Cells were transiently transfected at a density of 3 x 10^6 cells/mL using linear polyethylenimine (Polysciences Cat# 23966-1). 24-hours following transfection, media was supplemented with 2.2 mM valproic acid and expression carried out for 3-5 days at 37°C, 8% CO2. Supernatant was harvested from cells expressing spike ectodomains by centrifugation and filtered through a 0.22 μM filter prior to loading onto a 5 mL HisTrap excel column (Cytiva). The column was washed for 20 CVs with wash buffer (20 mM Tris pH 8.0, 500 mM NaCl), 5 CVs of wash buffer supplemented with 20 mM imidazole and the protein eluted with elution buffer (20 mM Tris pH 8.0, 500 mM NaCl, 500 mM imidazole). Elution fractions containing the protein were pooled and concentrated (Amicon Ultra 100 kDa cut off, Millipore Sigma) for gel filtration. Gel filtration was conducted using a Superose 6 10/300 GL column (Cytiva) pre-equilibrated with GF buffer (20 mM Tris pH 8.0, 150 mM NaCl). Fractions of the main protein peak (eluting at ~11 mL) were pooled and concentrated to 4.5 - 5.5 mg/mL (Amicon Ultra 100 kDa cut off, Millipore Sigma). Protein samples were immediately flash-frozen in liquid nitrogen and stored at -80°C.

Antibody production

VH-FC ab8, IgG ab1 and IgG CR3022 were produced as previously described (Li et al., 2020a, 2020b). Plasmids encoding light and heavy chains for Fab S309 and S2M11 were synthesized (Synbio). Heavy chains were designed to incorporate a C terminal 6x histidine tag. Expi293 cells were transfected at a density of 3 x 10^6 cells/mL using linear polyethylenimine (Polysciences Cat# 23966-1). 24-hours following transfection, media was supplemented with 2.2 mM valproic acid and expression carried out for 3-5 days at 37°C, 8% CO2. The supernatant was harvested by centrifugation and filtered through a 0.22 μM filter prior to loading onto a 5 mL HisTrap excel column (Cytiva). The column was washed for 20 CVs with wash buffer (20 mM Tris pH 8.0, 500 mM NaCl), 5 CVs of wash buffer supplemented with 20 mM imidazole and the protein eluted with elution buffer (20 mM Tris pH 8.0, 500 mM NaCl, 500 mM imidazole). Elution fractions containing the protein were pooled and concentrated (Amicon Ultra 10 kDa cut off, Millipore Sigma) for gel filtration. Gel filtration was conducted using a Superose 6 10/300 GL column (Cytiva) pre-equilibrated with GF buffer (20 mM Tris pH 8.0, 150 mM NaCl). Peak fractions corresponding to soluble protein were pooled and concentrated to 8 - 20 mg/mL (Amicon Ultra 10 kDa cut off, Millipore Sigma). Protein samples were stored at 4°C until use.

Electron microscopy sample preparation and data collection

S-protein samples were prepared at 2.25 mg/mL, with and without the addition of ACE2 (~1:1.25 S-protein trimer:ACE2 molar ratio) (New England Biolabs). Vitrified samples of S-protein constructs with and without ACE2 were prepared by first glow discharging Quantifoil R1.2/1.3 300 mesh holey carbon copper grids for 1 minute using a Pelco easiGlow glow discharge unit (Ted Pella) and then applying 1.8 μL of protein suspension to the surface of the grid. Grids were blotted (12 sec, blot force -10) and plunge frozen into liquid ethane using a Vitrobot Mark IV (Thermo Fisher Scientific) at a temperature of 10°C and a humidity level of 100%. All cryo-EM samples were imaged using a 300 kV Titan Krios G4 transmission electron microscope (ThermoFisher Scientific) equipped with a Falcon4 direct electron detector in electron event registration (EER) mode. Movies were collected at 155,000x magnification (physical pixel size 0.5 Å) over a defocus range of -0.5 μm to -3 μm with a total dose of 40 e-/ $Å^2$ using EPU automated acquisition software.

Image processing

In general, all data processing was performed in cryoSPARC v.3.0.1 (Punjani et al., 2017) unless stated otherwise. Motion correction in patch mode (EER upsampling factor 1, EER number of fractions 40), CTF estimation in patch mode, reference-free particle picking and particle extraction were performed on-the-fly in cryoSPARC. After preprocessing, particles were subjected to 2D classification and/or 3D heterogeneous classification. Final 3D refinement was done with per particle CTF estimation and aberration correction. For complex of spike protein ectodomain and human ACE2, focused refinements were performed with a soft mask covering single RBD and its bound ACE2. Global resolution and focused resolution were according to the gold-standard FSC (Bell et al., 2016).

Model building and refinement

For models of spike protein ectodomain alone, SARS-CoV-2 HexaPro S trimer with N501Y mutation (PDB code 7MJG) were docked into cryo-EM density using UCSF Chimera v.1.15 (Pettersen et al., 2004). Then mutation and manual adjustment were done with COOT v.0.9.3 (Emsley et al., 2010), followed by iterative rounds of refinement in COOT and Phenix v.1.19 (Afonine et al., 2018). Glycans were added at N-linked glycosylation sites in COOT. For models of complex of spike protein ectodomain and human ACE2, the RBD-ACE2 subcomplex was built using coordinates of PDB code 7MJN as initial model and refined against focused refinement maps. Then it was docked into global refinement maps together with individual domains of spike protein. Model validation was performed using MolProbity (Chen et al., 2010). Figures were prepared using UCSF Chimera, UCSF ChimeraX v.1.1.1 (Goddard et al., 2018), and PyMOL (v.2.2 Schrodinger, LLC).

Biolayer interferometry (BLI) S protein-ACE2 binding assay

The binding kinetics of SARS-CoV-2 trimers and human ACE2 was analyzed with the biolayer interferometer BLItz (ForteBio, Menlo Park, CA). Protein-A biosensors (ForteBio: 18–5010) were coated with ACE2-mFc (40 μg/mL) for 2 min and incubated in DPBS

(pH = 7.4) to establish baselines. Concentrations of 125, 250, 500 and 1000 nM spike trimers were used for association for 2 min followed by dissociation in DPBS for 5 min. The association (k_{on}) and dissociation (k_{off}) rates were derived from the sensorgrams fitting and used to calculate the binding equilibrium constant (K_D).

Enzyme-linked immunosorbent assay (ELISA)

100 μl of wild-type or VoC RBD mutant SARS-CoV-2 S protein preparations were coated onto 96-well MaxiSorp™ plates at 2 μg/ml in PBS overnight at 4°C. All washing steps were performed 5 times with PBS + 0.05% Tween 20 (PBS-T). After washing, wells were either incubated with blocking buffer (PBS-T + 2% BSA) for 1 hr at room temperature. After washing, wells were incubated with dilutions of primary antibodies in PBS-T + 0.5% BSA buffer for 1 hr at room temperature. After washing, wells were incubated with goat anti-human IgG (Jackson ImmunoResearch) at a 1:8,000 dilution in PBS-T + 0.5% BSA buffer for 1 hr at room temperature. After washing, the substrate solution (Pierce™ 1-Step™) was used for colour development according to the manufacturer's specifications. Optical density at 450 nm was read on a Varioskan Lux plate reader (Thermo Fisher Scientific).

Analysis of convalescent patient antibody footprints

PDB entries of SARS-CoV-2 spike or RBD complexes with antibody fragments isolated from convalescent patients were selected. Antibody footprints were determined by consulting respective depositing studies along with analysis of protein-protein contacts using PDBsum (Laskowski et al., 2018).

QUANTIFICATION AND STATISTICAL ANALYSIS

The Area under the curve (AUC) for ELISA binding data was calculated in GraphPad Prism 7. No statistical analysis was performed in this study.